Forthcoming Articles have been peer-reviewed and accepted for publication in *InterPore Journal*. To make research available as early as possible, accepted manuscripts may be published online prior to completion of the final production process. These versions have not yet undergone final formatting, proofreading, or author corrections and therefore do not represent the **Version of Record**. Minor changes may occur during the final production process. The article will be updated with the final Version of Record when it is published in its assigned journal issue. **Forthcoming Articles should be cited using their DOI, which will remain the same after publication of the final Version of Record.**

Please cite the following article as:

Karibi-Botoye, N. F., Theraulaz, G., Muljadi, B., Demyanov, V., & Singh, K,. (2026). Multiscale structural control of airflow, diffusion and heat transfer in non-fungus farming termite mounds. InterPore Journal. Forthcoming Article.
https://doi.org/10.69631/1x1hh585

Received on: 21 Apr. 2026
Accepted on: 31 Aug. 2026
Published online (Accepted version): 16 Sep. 2026

Multiscale structural control of airflow, diffusion and heat transfer in non-fungus farming termite mounds

Nengi F Karibi-Botoye[1], Guy Theraulaz[2], Bagus Muljadi[3], Vasily Demyanov[1] & Kamaljit Singh[1]

[1] Institute of GeoEnergy Engineering, School of Energy, Geoscience, Infrastructure & Society, Heriot-Watt University, EH14 4AS Edinburgh, United Kingdom.

[2] Centre de Recherches sur la Cognition Animale (CRCA), Centre de Biologie Intégrative (CBI), Université de Toulouse, CNRS, UPS, Toulouse, France.

[3] Department of Chemical and Environmental Engineering, University of Nottingham, NG7 2RD Nottingham, United Kingdom.

Abstract

Termite mounds exhibit highly heterogeneous porous architectures that support efficient ventilation and thermoregulation under variable environmental conditions. Despite considerable interest, particularly in the context of bio-inspired design, the structural properties governing these processes remain only partially understood. In this study, we combine X-ray tomography and numerical simulations to investigate the relationship between structure and climatic properties in non-fungus farming termite mounds built by species from the genera *Trinervitermes*, *Cubitermes*, *Apicotermes*, and *Thoracotermes*. Our results reveal substantial variation in airflow, diffusive transport, and thermal behaviour within mound interiors, driven by differences in internal architecture. At the scale of the whole mound, transport appear to be strongly constrained by the outer walls, which act as the primary resistance to flow and diffusion, thereby largely determining overall permeability and CO_2 diffusivity. At the microscale, wall microporosity plays a key role in determining both CO_2 diffusion and thermal conductivity, with increased microporosity enhancing gas exchange while reducing heat transfer. Within the mound interior, however, connectivity, porosity and tortuosity emerge as the principal structural factors influencing transport. Together, these findings indicate that transport in termite mounds is inherently multiscale, with microscale wall properties exerting a strong influence on macroscale behaviour. This work advances understanding of the mechanisms underlying passive ventilation and heat transfer in termite mounds and offers potential guidance for the design of energy efficient, bio-inspired systems.

Keywords: Thermoregulation, ventilation, diffusion, termite mounds, X-ray tomography, numerical simulation, permeability, thermal conductivity, CO_2 diffusivity, heat transfer, climate control.

1. Introduction

Termite mounds are complex biogenic structures that have long attracted attention from both scientists and architects due to their remarkable integration of form and function (1). These structures maintain relatively stable thermal, humidity, and ventilation conditions despite strongly fluctuating external environments (2,3). Replicating such passive regulatory mechanisms in human-built systems could improve energy efficiency and reduce CO_2 emissions by lowering energy demand (4). Achieving this goal, however, requires a detailed understanding of the physical processes governing transport within the mound as well as the structural features that enable and regulate these processes. An interdisciplinary approach combining X-ray tomography and numerical simulations provides deeper insight into the coupling between structure and transport, thereby advancing beyond traditional, predominantly biologically oriented analyses (4).

Termite mounds are constructed from a mixture of soil, saliva, wood fragments, and faecal material (5–8), resulting in mechanically robust structures that can persist for decades to centuries (7,9,10). Termites exhibit high taxonomic diversity, comprising approximately 297 genera and 2951 species (11), and display a wide range of mound architectures that vary in size, geometry, and colony scale (2,12–14). Previous studies have shown that termite mounds are composed of four principal zones: the outer mantle, transition zone, accumulation zone, and nest (15). Chemical pheromones, environmental cues, vibrational cues, and social interactions have all been proposed as factors influencing the mound construction process (16–18).

Mounds are broadly classified into fungus farming and non-fungus farming types. Fungus farming species cultivate symbiotic *Termitomyces* fungi and must maintain tightly regulated thermal and humidity conditions to support fungal growth, whereas the fungi contribute to nutrient processing for the colony. In contrast, non-fungus farming termites do not maintain fungal gardens and are therefore subject to different environmental and physiological constraints.

The mechanisms responsible for ventilation and thermoregulation in termite mounds continue to be an active area of research. Several mechanisms have been proposed to explain ventilation, including wind-driven ventilation (19,20), the Venturi or stack effect in open mounds (21), thermally driven convection arising from diurnal temperature fluctuations (3,22) and diffusion through the porous mound structure (23). In fungus farming termite mounds, extensive ventilation networks, and heterogeneous thermal mass have often been associated with convective airflow and bulk gas exchange. In contrast, diffusion through the porous mound structure has been suggested to play a greater role in smaller termite mounds lacking large scale ventilation shafts. The relative importance of these mechanisms is expected to depend on mound architecture, environmental conditions, and termite ecology.

Direct measurements of airflow within termite mounds remain limited, particularly for non-fungus farming species. This is due to several factors, including the low air velocities within the mounds, which are often below the measurement range of commercially available instruments, the opaque nature of the mound material, and the hostility of the mound environment when termites are present (3). In contrast, thermoregulation in termite mounds is better understood, with factors such as outer wall thickness and mound size identified as important parameters influencing thermoregulation (24,25).

Non-fungus farming termite mounds are generally smaller than fungus farming mounds and do not require the maintenance of environmental conditions suitable for fungal growth. At the millimetre scale, these mounds consist of a network of chambers (channels) corresponding to void spaces within the structure, separated by inner and outer walls. At microscale, the walls are composed of a porous matrix of sand, clay, and mineral components (see Figure 3 in Karibi-Botoye *et al*. (4)). Transport processes in non-fungus farming mounds may differ from those observed in the well-studied *Macrotermes* systems. However, despite their diversity and ecological importance, non-fungus farming mounds remain considerably less studied.

Previous studies have characterized these non-fungus termite mound structures using X-ray imaging, graph-based approaches, and in situ measurements (25–29). However, numerical investigations of transport processes in non-fungus farming mounds remain limited. Existing work has largely focused on microscale analyses of the wall structure in *Trinervitermes geminatus* (19), leaving the multiscale coupling between structure and transport at the level of the whole mound largely unexplored.

Several important questions therefore remain unresolved. First, the relative importance of outer wall properties and internal mound architecture in controlling airflow, diffusion, and heat transfer is not well established in non-fungus termite mounds. Second, the transport properties of the wall microstructure remain poorly characterized. Finally, most previous studies have not explicitly linked microscale wall properties with mound scale transport, limiting our understanding of how wall microstructure influences overall mound performance.

This study focuses on non-fungus farming species, from the genera *Trinervitermes*, *Cubitermes*, *Apicotermes*, and *Thoracotermes*. It combines X-ray tomography with numerical simulations at multiscale levels to investigate how mound architecture influences diffusion, airflow, and heat transport in non-fungus farming termite mounds. Within the multiscale framework, microscale wall properties are explicitly upscaled and incorporated into millimetre-scale mound geometries, enabling the quantification of cross scale interactions between structural features and transport processes. To our knowledge, this represents the first application of combined millimetre scale and multiscale numerical simulations to these systems. The study addresses two main questions for non-fungus farming termite mounds: (1) what structural features enhance ventilation and heat transfer at millimetre scale? and (2) how do microscale wall properties influence transport behaviour observed at the millimetre scale?

We first describe the materials and methods used for the study including imaging and numerical simulation approaches. This is followed by the results section, which initially examines transport processes within the inner mound structure and subsequently assesses the influence of outer walls and wall microporosity on airflow and heat transport. The implications of these findings are then discussed in relation to the research questions, followed by a concluding section.

2. Materials and Methods

The dataset comprises two mounds of *T. geminatus*, six of *Cubitermes* spp., two of *Apicotermes* (including *Apicotermes lamani* and *Apicotermes* sp.), and three of *Thoracotermes* (including *Thoracotermes macrothorax* and *Thoracotermes* sp.). These species were selected to enable comparison with previously studied systems. All sampled mounds correspond to epigeal structures, with the exception of *Apicotermes*, which constructs fully subterranean mounds.

Samples were collected from multiple regions in Africa, including Guinea, Senegal, Congo, and Cameroon. The mounds were imaged using X-ray tomography at the millimetre scale, with voxel resolutions ranging from 0.3 to 0.85 mm. The resulting three-dimensional datasets were subsequently used as input geometries for numerical simulations. Detailed descriptions of imaging, data processing, and simulation procedures are provided below.

2.1 X-ray tomography and image analysis

2.1.1 Millimetre scale imaging and image processing

The four termite mound species were scanned using a medical X-ray computed tomography (CT) system (Somatom Sensation 16, Siemens, Erlangen, Germany) operated at 120 kV and 150 mA, with voxel sizes ranging from 0.3 to 0.85 mm. Representative three-dimensional reconstructions are shown in Figure 1.

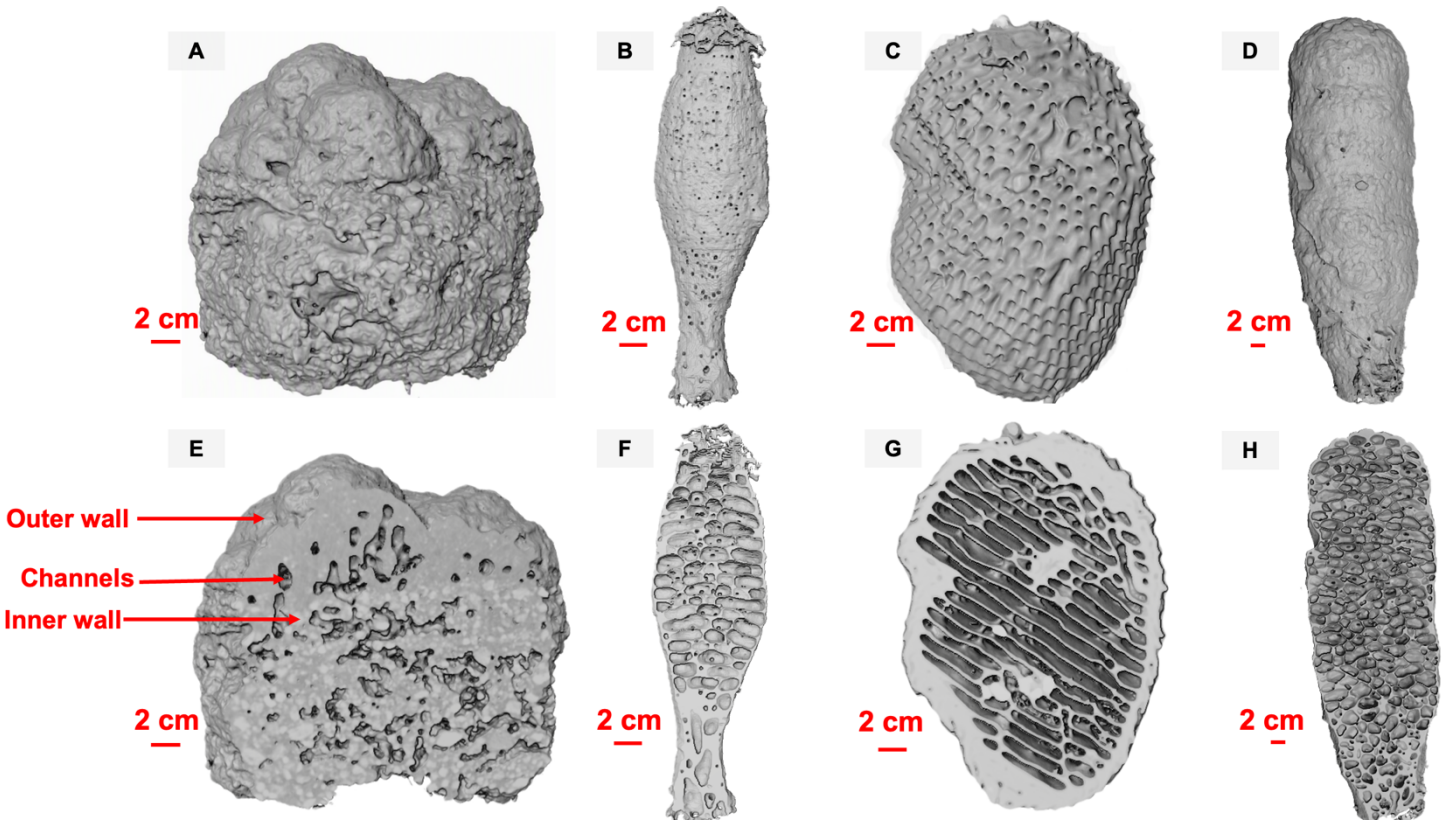

Figure 1: CT reconstructions of non-fungus farming termite mounds. (A) Trinervitermes geminatus mound, (B) Cubitermes mound, (C) Apicotermes mound, (D) Thoracotermes mound. (E–H) Corresponding views of the internal architecture following vertical clipping of the 3D reconstructions. The Apicotermes mound exhibits millimetre-scale openings distributed across the outer wall.

Following acquisition, all datasets were processed to enhance image quality and prepare them for quantitative analysis. Noise reduction was first performed using a non-local means filter (30,31) implemented in Avizo. Image segmentation was then carried out using either watershed methods or the Weka segmentation tool in ImageJ. The images were segmented into solid and air phases with an additional external air phase when present, as described in (4). Subsequent morphological operations, including dilation, erosion, and mask generation, were applied as needed to refine phase boundaries and ensure consistency across datasets. For *Trinervitermes*, *Cubitermes,* and *Thoracotermes* mounds only the epigeal portions of the structures were retained for further analysis.

Prior to analysis, all images were resampled in Avizo using the Box or Lanczos option to ensure the same voxel size in all three spatial directions as was required by the numerical solver. Differences in porosity between original and resampled images remained below 5%, indicating that the resampling procedure preserved the essential structural features. A representative elementary volume (REV) analysis was performed on the inner regions of mounds (defined here as the internal domains composed of channels and inner walls) prior to numerical simulations. This approach follows the statistical REV (sREV) method in which a cubic window is translated throughout the image while its size is progressively increased until the property of interest converges to a stable value. The properties analysed were the porosity and permeability.

To account for the influence of outer walls on flow and heat transport, artificial outer walls were manually appended to the inner mound sections. This step was necessary because full mound scans included surrounding air, and the geometric complexity of the structures prevented the direct extraction of a computational domain corresponding solely to the mound structure. The outer walls were added along the primary flow direction (x-direction), as shown in Figure 2. The appended outer walls were constructed to reproduce the main characteristics of the natural outer walls relevant to transport processes within the mound. The wall thickness was chosen such that the ratio between the size of the inner section and the outer wall thickness was consistent with that observed in the original mound CT image. In the multiscale simulations, effective wall properties obtained from previous microscale simulations of termite mound walls were assigned to the appended walls. Comparison of the original termite mound geometry and the reconstructed subvolume with the appended outer wall used in the multiscale simulations for *Thoracotermes* (M1-TH) is shown in the supplementary material (Figure S1).

For the *Apicotermes* mound, millimetre-scale holes were incorporated into the outer walls to reproduce their natural architecture. These holes are reported to be small, evenly spaced, and impermeable to termite passage (5). This feature was implemented using hole diameters of less than 3 mm, consistent with observational data (Figure 2).

Outer walls were incorporated into a limited number of subvolumes (two per species), as the construction procedure was manual and computationally demanding. The selected subvolumes were considered representative of the analysed mound regions and were used to investigate the influence of outer wall properties on transport. The objective of these simulations was not to quantify variability within each mound or species, but rather to investigate the influence of outer walls on transport in representative mound structures.

While the appended walls do not capture local variations in wall thickness, fine-scale structural heterogeneity, or all geometric features of the natural outer walls, they provide a simplified representation of the outer wall structure and transport properties suitable for investigating airflow, CO_2 diffusion, and heat transfer at the mound scale. Furthermore, even if the complete outer wall geometry had been extracted from the millimetre-scale CT images, microscale features such as microporosity and pore connectivity would not have been resolved at the image resolution used in this study and therefore still require representation through effective properties. As the relative outer wall thickness influences the predicted transport properties (see Figure 7B), the appended wall thickness was selected to preserve the ratio between the inner section and outer wall thickness observed in the original CT images. Consequently, the simulated transport properties should be interpreted in the context of the outer wall geometry adopted in this study.

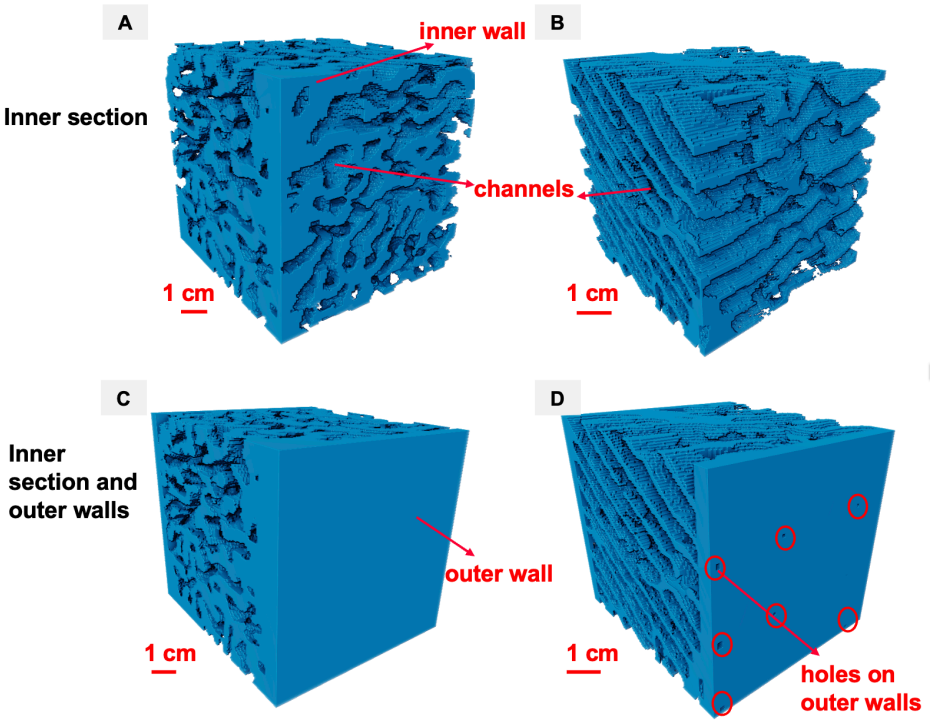

Figure 2: Construction of computational domains by integrating outer walls with inner mound sections for different termite species. (A) Inner section of T. geminatus (B) Inner section of Apicotermes. Inner sections (comprising channels and inner walls) were extended by adding outer wall layers along the principal flow direction (x-direction) to reproduce full mound configurations. Two types of outer wall structures are shown: (C) Non-perforated walls representative of T. geminatus and (D) Perforated walls with millimetre-scale openings representative of Apicotermes. The perforations are regularly distributed and implemented with diameters smaller than 3 mm, consistent with observed structural features.

2.1.2 Image analysis

Image analysis was performed to quantify key architectural features of the termite mounds, including porosity, height, volume, Euler number, connectivity, and channel thickness. All analyses were conducted using Avizo software. The height and maximum diameter of each sample were measured using the line measurement tool. Porosity was computed as the ratio of air volume to total volume (air and solid phases), based on voxel counts. Tortuosity was determined using the centroid path tortuosity module (32). The integral mean curvature, which quantifies the overall surface curvature of the structure, was computed using the curvature integral module in Avizo. The Euler number, providing a topological measure of connectivity, was computed in 3D as

$$\chi = \beta_0 - \beta_1 - \beta_2 \quad (1)$$

where β_0 is the number of connected components, β_1 is the number of holes, and β_2 is the number of enclosed cavities.

Channel and wall thicknesses were determined by assigning a value of 1 to the phase of interest and the rest of the phases as zero, followed by application of the thickness map module, which computes the diameter of the largest sphere that can be inscribed at each voxel. Connectivity was evaluated using the axis connectivity module, and the fraction of connected structures was quantified as the ratio of connected volume to total volume. Unless otherwise stated, the structural properties reported in this study refer to the millimetre-scale mound architecture extracted from the CT images. For example, porosity refers to the fraction of pore space occupied by channels and chambers within the analysed volume, whereas wall microporosity is stated explicitly when discussed.

2.2 Numerical simulation

Simulations were performed using GeoChemFoam, an open-source solver based on OpenFOAM specifically designed for porous media applications (33). The velocity and pressure fields were obtained by solving the Darcy-Brinkman-Stokes (DBS) equations:

$$\frac{1}{\phi^2}\nabla.(u \otimes u) = -\nabla p + \frac{\nu}{\phi}\nabla^2 u - \nu K^{-1} u \quad (2)$$

$$K^{-1} = \frac{180\,(1-\phi)^2}{h^2\phi^3} \quad (3)$$

where u is the velocity vector, ν is the kinematic viscosity, p is the pressure, K is the permeability, ϕ is the porosity, and h is the mesh resolution.

Air was used as the working fluid, with a kinematic viscosity of 1.602×10^{-5} m^2s^{-1}. A volumetric flow rate of 1×10^{-7} m^3s^{-1} was imposed at the inlet of the mound, with zero-gradient boundary conditions at the outlet and no-slip conditions at the solid walls. Under these conditions, the Reynolds numbers remain $\ll 1$, corresponding to creeping flow within the Darcy regime and consistent with the low velocities reported in termite mounds (4).

For pressure, velocity and temperature simulations within the inner mound sections, a structured grid was used. The initial mesh resolution corresponded to approximately half the number of voxels in the image and was subsequently refined once to match the full voxel resolution. This approach reduced computational cost while maintaining accuracy, with deviations in permeability below 5% compared to simulations performed at full resolution.

For multiscale simulations of pressure and velocity, a similar grid strategy was adopted, with one notable exception. For the *Apicotermes* M1-A mound, each voxel was directly mapped to

a computational cell of equal size. This higher resolution was required due to the presence of perforated outer walls, as coarser grids resulted in permeability deviations of up to a factor of four. For the *Apicotermes* M4-A mound, however, full resolution simulations were computationally prohibitive, and the reduced resolution approach was therefore retained.

These simulations are referred to as multiscale, as effective wall properties (e.g., porosity and permeability) derived from microscale simulations were upscaled and assigned to the walls in the millimetre-scale models to represent mound-scale flow. The solid walls of the mounds were assigned a microporosity of 15% and a permeability of 2×10^{-12} m^2, based on microscale simulations reported by Singh et al. for *T. geminatus* mounds (29). These values were applied to all species because comparable microscale data are not currently available for other non-fungus farming termite mounds. Therefore, the focus of the multiscale simulations was on understanding the influence of outer wall properties on overall mound transport rather than comparing species based on their overall permeability, CO_2 diffusivity, or thermal conductivity. Consequently, the influence of species-specific wall microstructure on mound scale transport could not be assessed in the present study.

Cyclic boundary conditions were applied at the inlet and outlet in the multiscale simulations of pressure and velocity, while zero-gradient conditions were imposed at the walls. The applied pressure drop corresponded to an equivalent flow rate of 1×10^{-7} m^{3}s^{-1}.

The permeability across the mounds was determined using Darcy's equation:

$$K = -\frac{\nu L_D\, u}{\Delta P} \tag{4}$$

where ΔP is the pressure drop between inlet and outlet, L_D is the full length of the domain (33).

Thermal conductivity under steady state is described by

$$0 = \nabla.(k\nabla \mathrm{T}) \tag{5}$$

where T is temperature.

The thermal conductivity can be calculated from the harmonic average of thermal conductivity of each phase weighed by its volume fraction (Equation 6) or arithmetic average (Equation 7).

$$k = \frac{k_f k_s}{(1-\phi)k_f + \phi k_s} \tag{6}$$

$$k = \phi k_f + (1 - \phi) k_s \quad (7)$$

where k_f is thermal conductivity of the fluid and k_s is the thermal conductivity of the solid.

Harmonic averaging corresponds to a configuration in which heat transfer occurs sequentially across phases along the direction of heat flow, thereby providing a lower bound for the effective thermal conductivity, whereas arithmetic averaging assumes preferential heat flow through the more conductive phase, and therefore represents an upper bound (34). The solid pore structure of the mound walls is highly heterogeneous and cannot be adequately represented by either idealised configuration alone. Therefore, the effective thermal conductivity was estimated as the mean of the harmonic and arithmetic bounds, yielding a value constrained within these limits.

The solid walls were assigned a thermal conductivity of 6.3 W/m·K, a specific heat capacity of 767.64 J/kg·K, and a density of 3003.16 kg/m³. These values were derived from the arithmetic weighted average of the mineral composition of the Guinea mound reported by Singh *et al*. (29). Arithmetic averaging was adopted to reflect the high connectivity of the solid phase within the mound structure. Detailed mineralogical information and precise collection locations were not available for the remaining mound samples and therefore species-specific thermal properties could not be assigned. As soil mineralogy may vary between geographical regions, the assumed solid phase thermal properties may influence the predicted thermal conductivity values. A sensitivity analysis examining the influence of solid phase thermal conductivity on the apparent thermal conductivity is provided in the supplementary material (Figure S2).

For the thermal simulations, the temperature was set to 1 at the inlet and 0 at the outlet, with zero-gradient boundary conditions imposed at the walls. The initial temperature field was uniformly set to 1, and steady-state conditions were assumed.

CO_2 transport was modelled using Fick's second law under steady-state conditions:

$$0 = \nabla . (\phi D \nabla C) \quad (8)$$

where C is the concentration of the CO_2 and D is the diffusion coefficient.

For all CO_2 simulations, a structured grid was used in which each voxel was directly mapped to a numerical grid cell of equal size. This method could not be applied to *Apicotermes* M3_A

and M4_A because of computational constraints, and a reduced grid resolution corresponding to half the number of voxels overestimated diffusivity by 51% relative to the full resolution grid for the *Apicotermes* mound. Therefore, the CO_2 diffusivity values obtained for *Apicotermes* M3_A and M4_A were excluded from the subsequent analyses and interpretation.

The CO_2 concentration was set to 1 at the inlet and 0 at the outlet, with zero-gradient boundary conditions at the walls and an initial concentration field set to zero under steady-state conditions. In multiscale simulations, the setField option was used to assign CO_2 diffusivity values to the outer walls. For all mounds except *Apicotermes*, the outer wall diffusivity was set to 3.1×10^{-7} m^2s^{-1}, based on the microscale estimates reported by Singh *et al*. (29). This value was not applied to the *Apicotermes* mound because the outer-wall region contains both microporous wall material and millimetre-scale perforations. Using the setField approach would assign a single diffusivity to the entire region, including the perforations. Instead, only the wall porosity was assigned, allowing CO_2 diffusion through both the porous wall and the millimetre-scale perforations.

For the multiple regression analysis of the results, models were evaluated for normality of residuals, homoscedasticity, and multicollinearity. The results of the regression diagnostics are provided in the supplementary material (Table S2). A power-law formulation was adopted for permeability and CO_2 diffusivity, as it improved predictive performance. For thermal conductivity, surface area was excluded due to its strong correlation with volume, integral mean curvature and Euler number were omitted because it had a negligible effect on the coefficient of determination (R^2) and introduced heteroscedasticity. To assess the relative importance of each structural predictor, the impact on R^2(%) was calculated as the percentage change in the coefficient of determination after removing a predictor from the full regression model. Negative values indicate a reduction in R^2 relative to the full regression model:

$$\text{Impact on } R^2\ (\%) = \frac{R^2_{without\ predictor} - R^2_{full}}{R^2_{full}} \times 100 \quad (9)$$

where R^2_{full} is the coefficient of determination of the complete regression model and $R^2_{without\ predictor}$ is the coefficient of determination obtained after removing the predictor of interest from the model.

3. Results and discussion

We investigated the mounds of *T. geminatus*, *Cubitermes*, *Apicotermes*, and *Thoracotermes*. X-ray imaging of the inner sections reveals marked differences in their internal architectures. *Cubitermes* and *Thoracotermes* mounds are characterized by relatively large, bubble-like chambers, whereas *Apicotermes* and *T. geminatus* are characterized by thinner and more elongated channels (see Figure 1E - 1H). These architectural differences are associated with variation in chamber size, with larger chambers observed in *Cubitermes* and *Thoracotermes* compared to *Apicotermes* and *T. geminatus* (see Figure 7B in Karibi-Botoye *et al*. (4)). Across most mounds, the outer walls are thicker than the inner walls by a factor ranging from 1 to 3.3. In addition, channel dimensions generally exceed inner wall thickness, indicating that void space dominates the internal structure and forms a connected network of pathways for airflow and termite movement within the mound.

3.1 Flow and thermal properties in the inner section of the mound

The inner sections of the mound were characterized using a set of structural descriptors, including porosity, volume, tortuosity, channel thickness, inner wall thickness, and Minkowski functionals (volume (M0), surface area (M1), integral mean curvature (M2), and Euler characteristic (M3)). The complete dataset is provided in the supplementary material (Table S1). The inner sections exhibit high channel porosity, ranging from 0.31 to 0.78. *Apicotermes* mounds display the highest porosity, whereas *Cubitermes* exhibits the greatest variability. Channel connectivity exceeds 83% in most cases, with lower values observed in a few *Thoracotermes* mounds that were modified by smaller species, resulting in reduced porosity and connectivity. Velocity fields are spatially heterogeneous within the mounds, reflecting variations in channel architecture (see Figure 3E - 3H).

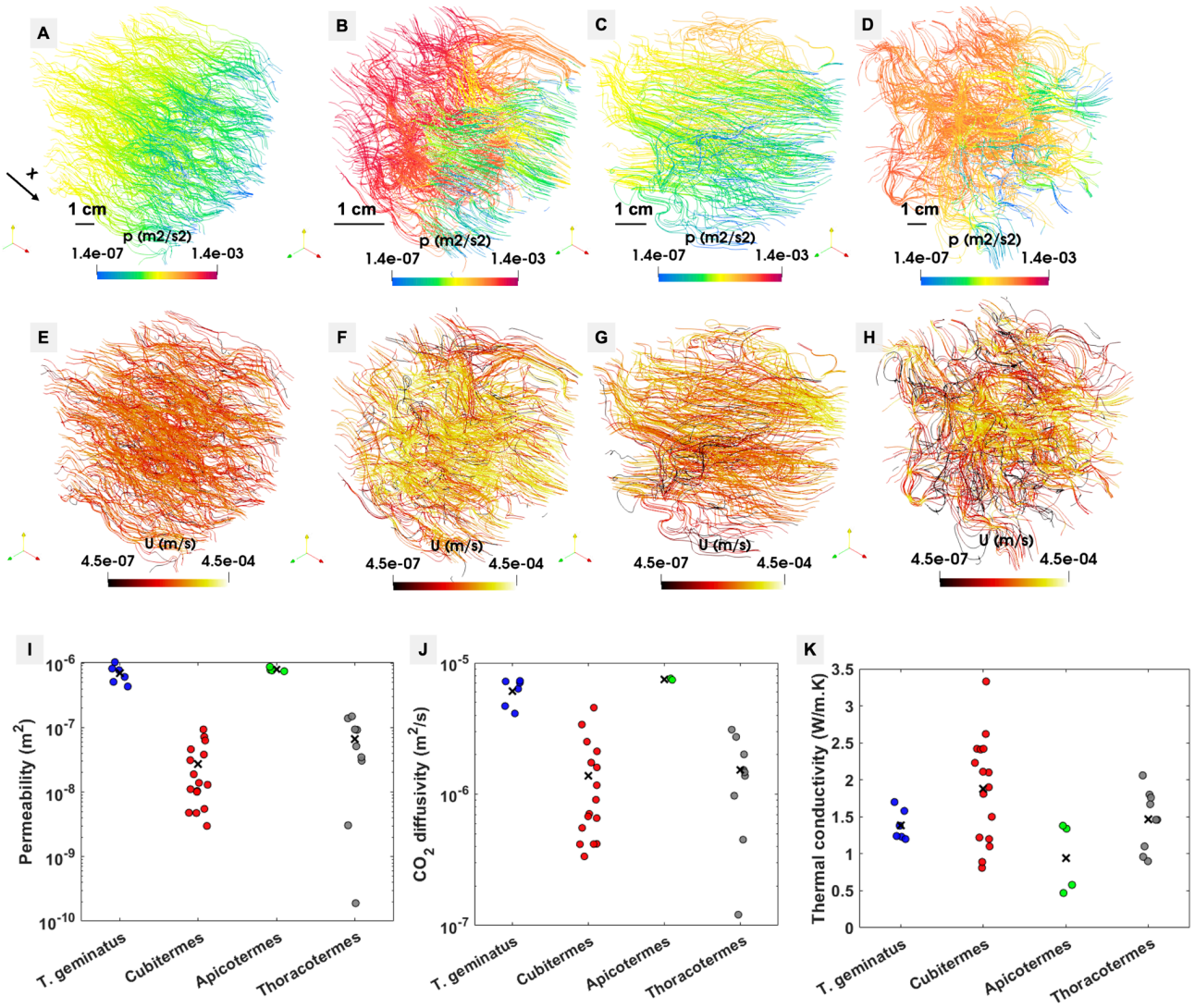

Figure 3: Flow fields and transport properties in the inner sections of non-fungus farming termite mounds. (A to D) Pressure fields and (E to H) Velocity fields for T. geminatus, cubitermes, Apicotermes and Thoracotermes respectively, (I) Permeability, (J) CO_2 diffusivity, and (K) Thermal conductivity for each mound type. Blue circles represent Trinervitermes geminatus, red circles Cubitermes, green circles Apicotermes, and grey circles Thoracotermes. Cross symbols indicate the mean value for each species. The arrow shows the direction of flow.

The permeability of the inner sections ranges from 1.9×10^{-10} to 1.63×10^{-6} m^2 (Figure 3I). The highest permeability values are observed in *T. geminatus* and *Apicotermes*, consistent with their higher porosity, greater connectivity, and lower tortuosity, which together reduce flow resistance. In contrast, *Cubitermes* and *Thoracotermes* exhibit lower permeability. The modified *Thoracotermes* mounds with reduced porosity and connectivity (M4-Th and M5-Th) display permeability values up to two orders of magnitude lower than those of other mounds within the same species.

386 *Table 1: Flow, diffusion and thermal properties within the inner section of non-fungus farming*
387 *mounds obtained from millimetre scale numerical simulations.*

Name of species	Subvolume ID	Permeability (m^2)	Average velocity (m/s)	CO_2 diffusivity (m^2/s)	Thermal conductivity (W/m.K)
T. Geminatus	M1_T	6.08E-07	8.93E-06	6.34E-06	1.4
	M2_T	7.73E-07	1.01E-05	7.06E-06	1.2
	M3_T	8.19E-07	8.19E-06	7.22E-06	1.2
	M4_T	1.03E-06	9.60E-06	7.29E-06	1.2
	M5_T	4.32E-07	1.92E-05	4.12E-06	1.7
	M6_T	5.10E-07	2.17E-05	4.69E-06	1.6
***Cubitermes* spp.**	M1_C	5.49E-09	3.60E-05	3.36E-07	2.4
	M2_C	1.39E-08	4.55E-05	7.09E-07	2.4
	M3_C	1.30E-08	5.95E-05	6.58E-07	2.6
	M4_C	3.12E-08	1.78E-05	1.60E-06	1.9
	M5_C	1.04E-08	3.77E-05	5.54E-07	2.2
	M6_C	4.60E-08	5.94E-05	2.12E-06	1.5
	M7_C	2.99E-09	5.68E-05	4.19E-07	2.1
	M8_C	4.79E-09	5.68E-05	6.77E-07	2.1
	M9_C	9.34E-08	4.00E-05	4.56E-06	0.8
	M10_C	7.19E-08	4.94E-05	3.39E-06	0.9
	M11_C	6.29E-08	1.11E-04	2.51E-06	1.2
	M12_C	1.11E-08	4.94E-05	9.08E-07	1.8
	M13_C	4.74E-09	8.17E-05	4.17E-07	2.4
	M14_C	1.89E-08	4.94E-05	1.17E-06	1.1
	M15_C	3.81E-08	4.00E-05	1.74E-06	1.2
	M16_C	1.01E-08	8.18E-05	4.16E-07	3.3
A. Lamani	M1_A	7.45E-07	1.87E-05	7.60E-06	0.5
	M2_A	7.78E-07	1.73E-05	7.42E-06	0.6
***Apicotermes* sp.**	M3_A	7.66E-07	2.17E-05		1.3
	M4_A	8.74E-07	2.17E-05		1.4
***Thoracotermes* sp.**	M1_Th	1.39E-07	7.55E-05	1.53326E-06	1.5
	M2_Th	3.06E-08	8.75E-05	1.38E-06	1.5
	M3_Th	5.13E-08	1.92E-05	1.47E-06	1.8
	M4_Th	1.90E-10	3.46E-05	1.21E-07	1.8
	M5_Th	3.06E-09	3.46E-05	4.51E-07	1.7
T. macrothorax	M6_Th	3.47E-08	1.76E-05	9.74E-07	2.1

Name of species	Subvolume ID	Permeability (m^2)	Average velocity (m/s)	CO_2 diffusivity (m^2/s)	Thermal conductivity (W/m.K)
	M7_Th	9.21E-08	1.14E-05	2.01E-06	1.1
	M8_Th	1.49E-07	1.14E-05	3.10E-06	0.9
	M9_Th	9.36E-08	1.03E-05	2.73E-06	1.0

CO_2 diffusivity ranges from 1.21×10^{-7} to 7.60×10^{-6} m^2s^{-1} (Figure 3J) and follows a similar trend to permeability, with the highest values observed in *T. geminatus* and *Apicotermes*. This correspondence likely arises because the same structural features that facilitate fluid flow, such as high porosity, strong connectivity, and low tortuosity, also promote CO_2 transport within the mounds.

Thermal conductivity ranges from 0.5 to 3.3 W/m·K across the mounds and exhibits an inverse relationship with both permeability and CO_2 diffusivity (Figure 3K). *T. geminatus* and *Apicotermes* display the lowest thermal conductivity values, whereas *Cubitermes* and *Thoracotermes* exhibit higher values. This trend indicates that more porous structures reduce heat transfer through the solid phase, thereby enhancing the insulating properties of the mound.

3.2 Influence of structural properties on transport behaviour in the inner section of the mound

To better understand the mechanisms controlling flow, diffusion, and heat transport within the inner mound sections, we examined the influence of key structural properties on these processes.

Porosity shows a generally positive relationship with permeability across most mounds, with higher porosity associated with increased permeability (Figure 4A). However, this relationship exhibits substantial scatter, indicating that permeability is not governed by porosity alone but also depends on the organisation of the void space. In particular, mounds with similar porosity can display markedly different permeability values due to variations in connectivity and tortuosity.

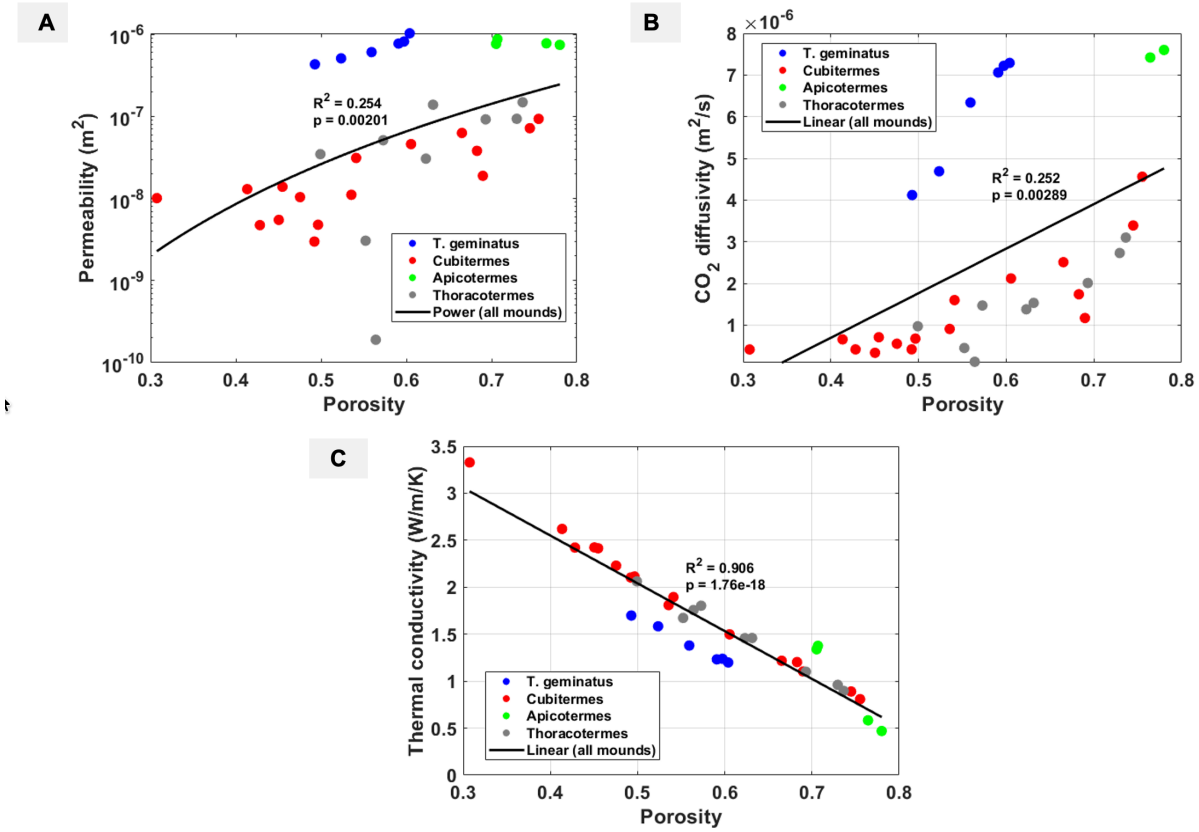

Figure 4: Relationships between porosity and transport properties in different mounds. (A) Porosity–permeability relationship, (B) Porosity–CO_2 diffusivity relationship, and (C) Porosity–thermal conductivity relationship. Points are coloured by species. The solid black lines represent regressions fitted to the combined dataset of all mound samples.

Similarly, CO_2 diffusivity shows a weak positive relationship with porosity (Figure 4B), with higher porosity associated with increased diffusivity as a result of more continuous and accessible transport pathways. However, considerable variability remains, indicating that porosity alone does not fully explain diffusive transport within the mounds. In contrast, thermal conductivity shows a stronger dependence on porosity, decreasing with increasing porosity (Figure 4C), reflecting the reduced contribution of the solid phase to heat transfer in more porous structures.

While porosity provides a useful first-order descriptor, it does not fully account for the observed variability in transport behaviour within the mounds. To address this limitation, the combined influence of multiple structural properties was assessed using multiple regression analysis. For permeability, the regression model is statistically significant ($p < 0.001$; $F(4,30) = 31.27$; $R^2 = 0.81$; $R^2adj = 0.78$), indicating that permeability is jointly controlled by channel connectivity, porosity, tortuosity, and inner wall thickness (Figure 5A). The adjusted

coefficient of determination (R^2adj) provides a measure of model fit that accounts for the number of predictors, reducing the risk of overfitting. Increased connectivity and porosity are associated with enhanced permeability, whereas higher tortuosity is associated with lower permeability because it increases the complexity of flow paths. The positive association between inner wall thickness and permeability likely reflects its correlation with more connected and porous channel networks rather than a direct effect of wall thickness. The equation relating permeability to the independent variables is provided in the supplementary material.

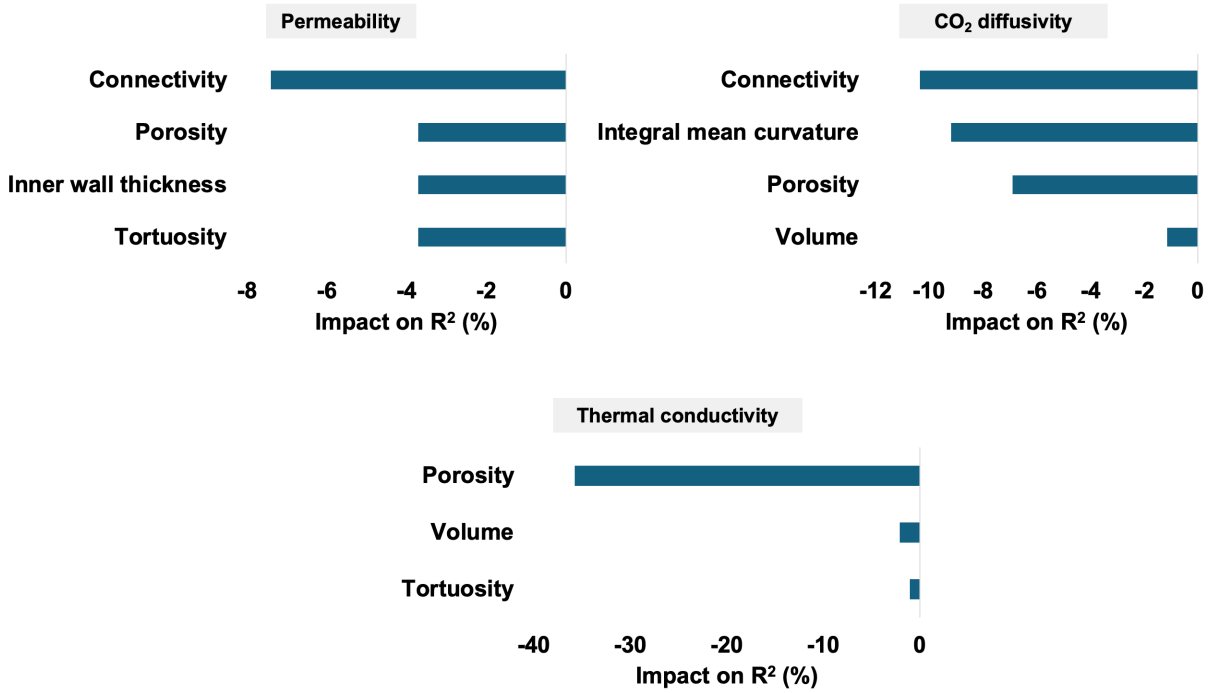

Figure 5: Relative influence of structural predictors on the coefficient of determination (R^2) of the regression models. Impact on R^2 (%) represents the percentage reduction in model R^2 following the removal of an individual predictor from the full model. (A) Permeability, (B) CO_2 diffusivity, and (C) thermal conductivity.

For CO_2 diffusivity, the regression model is also statistically significant ($p < 0.001$; $F(4, 28) = 46.44$; $R^2 = 0.87$; $R^2adj = 0.85$). Connectivity, porosity and integral mean curvature show the strongest associations with CO_2 diffusivity, with higher connectivity and porosity associated with increased diffusivity (Figure 5B). For thermal conductivity, porosity exhibits the strongest association, while other structural parameters show comparatively weaker relationships (Figure 5C). The corresponding regression model is also highly significant ($p < 0.001$; $F(3,31) = 216.68$; $R^2 = 0.95$; $R^2adj = 0.95$). Thermal conductivity decreases with increasing porosity, indicating greater resistance to heat transfer in more porous mound structures.

Overall, these results suggest that transport processes within termite mound interiors are governed by the combined effects of multiple structural properties rather than any single parameter. Porosity controls the available volume for transport, connectivity determines the degree to which these pore spaces are interconnected, and tortuosity controls the efficiency of transport by influencing the complexity of flow and diffusion pathways. Inner wall dimensions may further modulate these processes by affecting channel connectivity and local resistance within the structure. Together, these structural characteristics establish the balance between airflow, diffusive transport, and heat transfer within the mound.

3.3 Influence of outer walls on diffusion, airflow and heat transport through the mounds

Simulations of the inner sections (channels and inner walls) were extended to include outer walls in order to represent the full mound structure, following the methodology described in section 2. The outer walls were modelled as microporous layers with a porosity of 15%, permeability of 2×10^{-12} m^2 and CO_2 diffusivity of 3.1×10^{-7} m^2s^{-1}, based on Singh *et al*., (29). This approach yields a multiscale representation that couples millimetre-scale channels with microporous outer wall layers.

The porosity distributions for *T. geminatus* (with microporous outer walls) and *Apicotermes* mounds (with millimetre-scale wall perforations) are shown in Figure 6A and 6B, respectively. The resulting velocity fields are shown in Figure 6C & 6D. For mounds with microporous outer walls (Figure 6C), the velocity distribution closely resembles that observed in the inner sections without outer walls (see Figure 3E). In contrast, the *Apicotermes* mound exhibits more heterogeneous velocity fields due to the presence of millimetre-scale holes in the outer walls, which generate localised high velocity regions. The inclusion of outer walls leads to a substantial reduction in overall mound permeability (Figure 6E and Table 2), with decreases of up to five orders of magnitude observed in mounds with microporous walls. Despite significant differences in the permeability of the inner sections, the effective permeability of the full mounds converges to similar values across species, demonstrating that transport at the mound scale is primarily dominated by the outer walls.

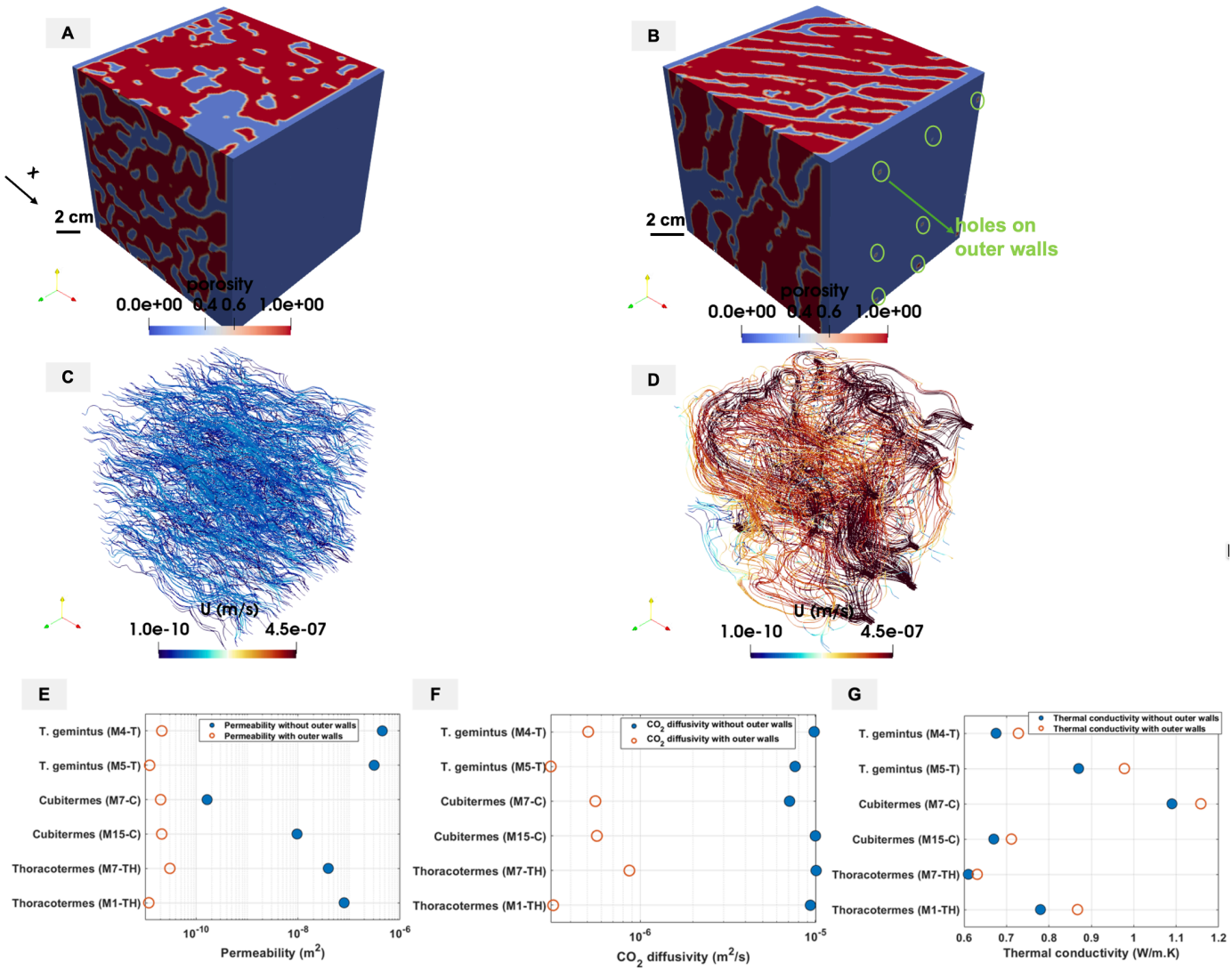

Figure 6: Numerical simulations of multiscale mound structures. (A) Porosity distribution in T. geminatus; (B) Porosity distribution in Apicotermes; (C) Velocity field in T. geminatus; and (D) Velocity field in Apicotermes. (E) Permeability, (F) CO_2 diffusivity, and (G) Thermal conductivity for different mounds with and without microporous outer walls. When present, both inner and outer walls have a microporosity of 15%.

494 *Table 2: CO_2 diffusivity, permeability and thermal conductivity in different mounds with outer*
495 *walls*

Species	Mound ID	Outer wall thickness (mm)	Length of mound (mm)	Porosity	Permeability (m^2)	CO_2 diffusivity (m^2/s)	CO_2 diffusivity (m^2/s) with micropores of 47% porosity	Thermal conductivity (W/m/K)	Thermal conductivity (W/m/K) with micropores of 47% porosity
T. geminatus	M4-T	5	112	0.6	2.12E-11	5.04E-07	1.49E-06	0.7	0.4
	M5-T	14	193	0.5	1.23E-11	3.08E-07	9.32E-07	1.0	0.6
***Cubitermes* spp.**	M7-C	2	46	0.5	2.01E-11	5.54E-07	1.64E-06	1.2	0.7
	M15-C	2	55	0.7	2.12E-11	5.65E-07	1.67E-06	0.7	0.4
A. lamani	M1-A	4	81	0.7	8.74E-11	8.57E-06	1.34E-05	0.3	0.2
***Apicotermes* sp.**	M4-A	2	73	0.7	3.32E-11			0.8	0.5
T. macrothorax	M7-Th	3	99	0.7	3.05E-11	8.66E-07	2.46E-06	0.6	0.4
***Thoracotermes* sp.**	M1-Th	3	43	0.6	1.18E-11	3.18E-07	1.00E-06	0.9	0.5

496

497 For mounds with microporous outer walls, the simulated permeability closely agrees with the
498 weighted harmonic average of the inner and outer sections, with values ranging from 0.9 to 1.1
499 times the predicted values. In contrast, *Apicotermes* mounds with millimetre-scale wall
500 openings deviate from this behaviour, as flow is preferentially channelled through these highly
501 permeable pathways rather than being uniformly distributed across the wall thickness.

502 Weighted harmonic average permeability (Equation 10) allows the relative contributions of the
503 inner section and outer walls to overall mound permeability to be quantified.

504 $$k = \frac{\sum_{i=1}^{n} x}{\sum_{i=1}^{n} \frac{x}{k}} \quad (10)$$

505 where x is thickness of the mound section and k = permeability of that section.

506 Using the weighted harmonic averaging approach (Equation 10) to calculate overall mound
507 permeability indicates that variations in the permeability of the inner sections have a negligible
508 impact on overall mound permeability. Increasing the inner section permeability by two orders
509 of magnitude results in only marginal changes. Similarly, reducing the inner section's
510 permeability by four orders of magnitude, comparable to the values observed in M4-Th and

M5-Th from mound 70 constructed by a smaller species, leads to a decrease in overall mound permeability of less than 10%.

In contrast, the properties of the outer wall appear to exert a dominant control. Doubling the outer wall permeability from 2×10^{-12} to 4×10^{-12} m^2 results in an approximately proportional increase in the overall mound permeability. Similarly, variations in layer thickness also significantly influence mound permeability. Increasing the thickness of the inner section while keeping other parameters constant leads to an increase in overall permeability, with a doubling of inner section thickness resulting in an approximately 1.9-fold increase. A similar effect is observed when the outer wall thickness is reduced. These results demonstrate that mound scale permeability is strongly governed by the properties of the outer walls and the relative thickness of structural layers. The influence of these parameters on overall mound permeability is shown in Figure 7A & 7B.

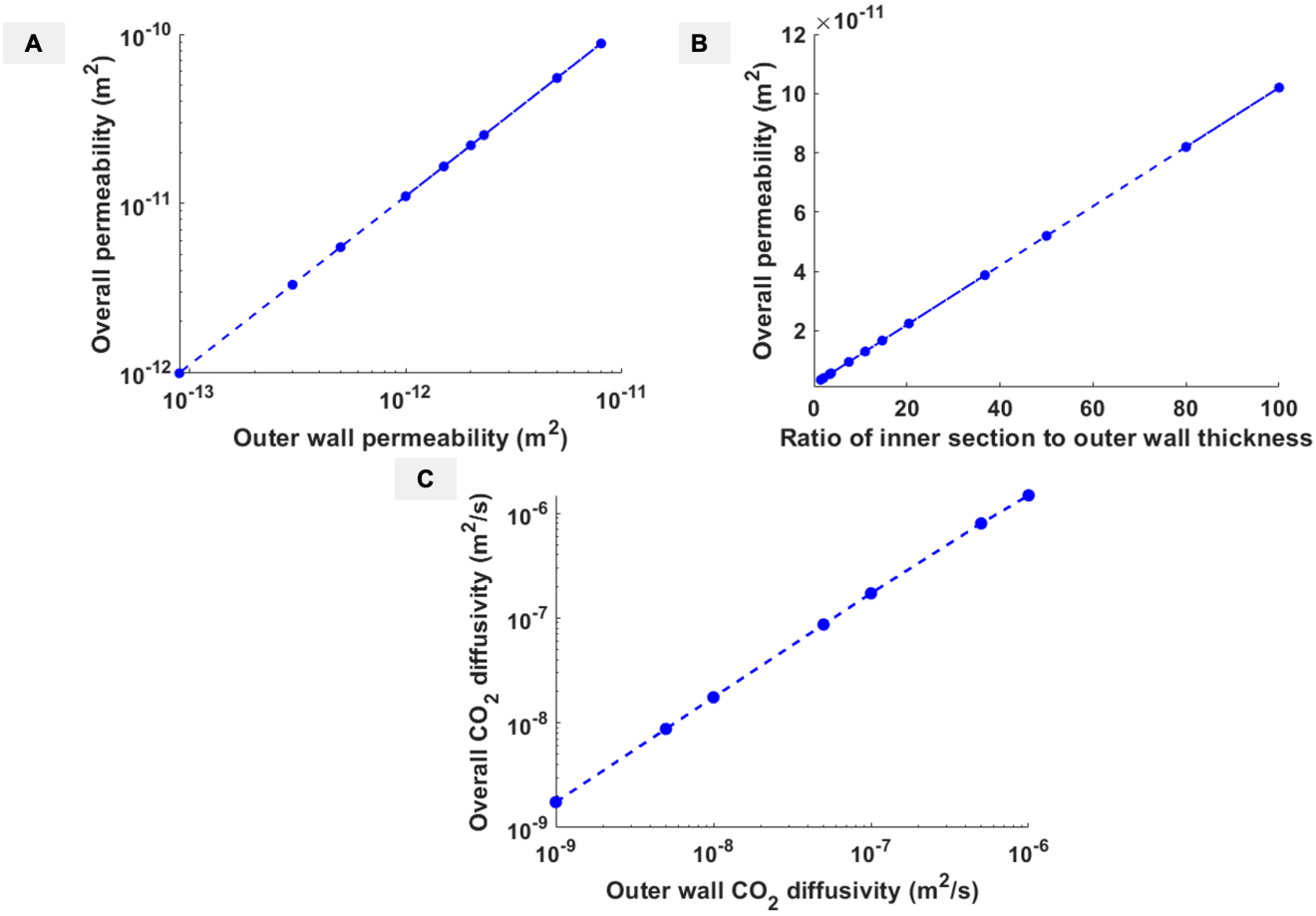

Figure 7: Sensitivity of overall mound transport properties to outer wall properties and structural layer thickness. (A) Effect of outer wall permeability on overall mound permeability; (B) Effect of the ratio between inner section thickness and outer wall thickness on overall mound permeability. (C) Effect of outer wall CO_2 diffusivity on overall mound diffusivity. Overall mound permeability was calculated using the weighted harmonic averaging approach

(Equation 10) and overall mound CO_2 diffusivity was based off numerical simulations. The data points represent the calculated (A–B) and simulated (C) values, while the dashed lines indicate the trend in the data points.

A similar trend is observed for CO_2 diffusivity when outer walls are included. The effective diffusivity is lower than that of the corresponding inner sections, with reductions of up to one order of magnitude (see Figure 6F). The overall CO_2 diffusivity appears to be strongly influenced by the properties of the outer wall, as the effective diffusivity of the entire mound closely approaches that of the outer walls (3.1×10^{-7} m²/s). This sensitivity to the outer wall CO_2 diffusivity is demonstrated in Figure 7C. In contrast, *Apicotermes* mound exhibits higher diffusivity due to the presence of millimetre-scale wall openings in the outer walls, which increase porosity and provide more direct diffusion pathways. This observation is consistent with the environmental conditions in which these mounds are typically found, often in humid soils where ventilation by diffusion is more constrained.

Thermal conductivity of mounds with outer walls ranges from 0.3 to 1.2 W/m·K (see Figure 6G) and exhibits a similar dependence on porosity as observed in the inner sections (see Figure 5C). Although the inclusion of outer walls increases the effective bulk thermal conductivity, the greater wall thickness may still improve insulation by increasing the distance over which heat must travel through the mound.

3.4 Influence of increasing microporosity on diffusion, airflow and heat transport in the mounds

In the preceding analysis, a default microporosity of 15% was used for the outer walls of the mounds. However, detailed measurements of wall microporosity are currently available only for *T. geminatus*, and comparable microscale data are lacking for the other species. It is therefore important to assess the sensitivity of airflow, diffusion, and heat transfer to variations in wall microporosity. To investigate this effect, the wall microporosity was increased to 47%, corresponding to the upper range of values reported in the literature for fungus farming termite mounds (3,35).

Increasing wall microporosity does not significantly alter the overall permeability of the mound, including in *Apicotermes* mounds that contain millimetre-scale openings. This is because the primary factors controlling permeability – namely outer wall permeability, inner section thickness, and outer wall thickness – remain unchanged during the simulations. A

similar trend is observed within the inner section of the mound, where permeability remains unchanged under the current assumptions.

In contrast, the CO_2 diffusivity increases by up to a factor of three as microporosity is raised from 15% to 47%, as shown in Figure 8A. The relative enhancement is more pronounced in mounds with lower initial CO_2 diffusivity, as additional micropores create new pathways for gas transport. This observation explains why *Apicotermes* mound exhibit a smaller increase (approximately 1.5-fold) as its CO_2 diffusivity is already high compared to the 2.95 – 3.03 -fold increases observed in the other mounds. Increasing microporosity also reduces the thermal conductivity of the mounds, by up to a factor of 1.5, as shown in Figure 8B. This reduction arises from a decrease in the solid phase, which constitutes the primary conducting phase of the mound. Consequently, increasing wall microporosity simultaneously enhances diffusive gas exchange while improving thermal insulation. These effects may be particularly advantageous for non-fungus farming termite mounds, where ventilation relies primarily on diffusion (27).

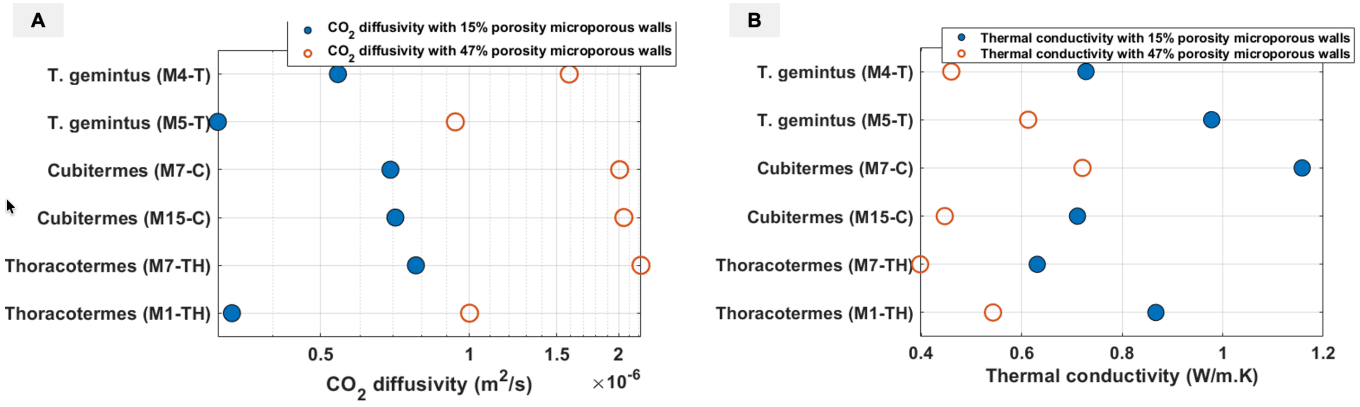

Figure 8: Influence of increasing outer wall microporosity on CO_2 diffusivity (A) and thermal conductivity (B) in non-fungus farming mounds. The microporosity is increased from 15% to 47% in these simulations.

To address the first research question —namely, which structural features enhance ventilation and influence heat transfer at the millimetre (mound) scale – the results indicate that these processes are influenced by structural features operating across multiple scales. At the mound scale, the outer walls appear to play the primary role in ventilation by governing gas exchange with the external environment. Their effective diffusivity, permeability, and thickness determine the magnitude of gas exchange. Within the mound interior, high channel porosity,

strong connectivity, and low tortuosity are associated with more efficient internal transport by promoting airflow and heat transfer.

With respect to the second research question, microscale properties appear to exert a dominant influence on millimetre-scale transport behaviour by determining the effective properties of the outer walls, which in turn govern overall mound performance. In particular, wall microporosity strongly influences CO_2 diffusivity and thermal conductivity, with higher microporosity enhancing diffusive transport while reducing thermal conductivity. These effects propagate across scales, leading to improved gas exchange and increased thermal insulation at the level of the entire mound.

Despite substantial variations in internal mound structure, the overall permeability is largely determined by the properties of the outer walls, indicating that microscale wall properties effectively define the boundary conditions for macroscale flow and diffusion. These findings show that transport behaviour in termite mounds is inherently multiscale, with microscale wall properties playing a key role in governing airflow, diffusion, and heat transfer at the mound scale.

4. Conclusion

Overall, the results suggest that the properties of the outer walls exert a strong influence on the transport of air and CO_2 in non-fungus farming mounds. Increasing outer wall permeability resulted in higher overall mound permeability in the simulations, while an increased inner section thickness relative to the outer walls thickness decreases resistance to transport and enhances flow. A similar relationship is observed for CO_2 diffusion, where higher outer wall diffusivity results in more efficient gas exchange across the mound. A key question is therefore which specific features most effectively enhance outer wall permeability and CO_2 diffusivity. For non-fungus farming mounds, where ventilation is predominantly diffusion driven, particular attention should be given to structural characteristics that maximise CO_2 diffusivity within the outer walls. Previous work by Singh *et al*. (29) dew Further work is required to determine which st ctural characteristics, in addition to pore size, most effectively enhance outer wall permeability and diffusivity.

Another important factor influencing CO_2 diffusivity and thermal conductivity is the amount of micropores within the mound walls. As microporosity increases, CO_2 diffusivity rises

accordingly due to the formation of additional flow pathways. In contrast, thermal conductivity decreases by up to a factor of 1.5 for a threefold increase in microporosity, as the fraction of the solid phase, the primary conductive medium, is reduced. These results demonstrate the multifunctional role of pore architecture. They also indicate that microscale wall properties have a strong influence on flow, diffusion, and heat transfer at the millimetre scale, highlighting the importance of characterizing wall microstructure in greater detail.

Characterizing the outer wall properties of different non-fungus farming species would also provide additional ecological context for the transport behaviour observed in different mound architectures. Such measurements would enable more representative multiscale simulations and allow differences in ventilation and heat transfer to be interpreted in relation to the ecological requirements of each species. Whether subterranean species such as *Apicotermes* exhibit distinct outer wall transport properties associated with subterranean environments remains an open question.

Although the outer walls appear to exert a strong influence on mound-scale transport, this does not imply that the inner sections of the mound are negligible. On the contrary, the inner sections must maintain sufficiently high permeability and CO_2 diffusivity to ensure efficient internal transport. Such properties can be achieved through increased channel connectivity and porosity combined with reduced tortuosity within the internal network. At the same time, maintaining relatively low thermal conductivity is advantageous for insulation, which is also strongly influenced by porosity.

The structural characteristics considered in this study should not be regarded as independent. In natural termite mounds, porosity, connectivity, tortuosity, and wall geometry are closely related, such that changes in one structural characteristic are likely to influence several others simultaneously. Although this study identifies the structural characteristics associated with transport behaviour, further work is required to isolate the influence of individual structural parameters.

Taken together, these results indicate that ventilation and heat transfer in non-fungus farming mounds are not governed by a single structural parameter but rather emerge from the combined effects of outer wall properties, wall microporosity, and internal architecture. The extent to which this transport principles apply beyond non-fungus farming termite mounds remains an

open question. In particular, comparisons with fungus farming termite mounds may help determine whether the influence of outer wall properties and microscale wall structure represents a general transport principle across termite taxa or is specific to mound architectures dominated by diffusion driven ventilation. Such comparisons may also provide further insight into the relationship between ecological function, mound architecture, and transport behaviour across different termite species.

Although the transport processes investigated here occur at the scale of termite mounds, similar processes occur in many biological and engineered porous systems. This study advances the understanding of ventilation and heat transfer in termite mounds by explicitly linking structural features across multiple scales. More broadly, the findings highlight that transport in biological porous systems is inherently multiscale, and that understanding the relationship between microscale structure and macroscale performance is essential not only for termite mounds but also for the design of natural and engineered porous materials. The multiscale framework developed here provides a means of systematically investigating how modifications to microscale wall architecture influence mound-scale transport behaviour and may also prove valuable for the design of hierarchical porous materials with tailored transport properties. Whether the multiscale transport principles identified in this study extend to larger engineered systems remains to be established. If shown to apply more broadly, these principles may provide new opportunities for the development of passive ventilation strategies for sustainable buildings and other engineered structures.

Acknowledgment

N.F.K. acknowledges Julien Maes and Hannah Menke for their help with the numerical simulations. N.F.K. and K.S. acknowledge funding from the James Watt Scholarship from Heriot-Watt University. N.F.K. acknowledges funding from Mary Burton funds from Heriot-Watt University. G.T. acknowledges funding from Agence Nationale de la Recherche (ANR-06-BYOS-0008) for X-ray medical scanning. G.T. also gratefully acknowledges the Indian Institute of Science to serve as Infosys visiting professor at the Centre for Ecological Sciences in Bengaluru, India.

Reference

1. Claggett, N., Surovek, A.E., Capehart, W.J. and Shahbazi, K., 2018. Termite mounds: Bioinspired examination of the role of material and environment in multifunctional structural forms. *Journal of Structural Engineering*, 144(7), p.04018068. https://doi.org/10.1061/(ASCE)ST.1943-541X.0002043.
2. Korb, J. and Linsenmair, K.E., 2000. Thermoregulation of termite mounds: what role does ambient temperature and metabolism of the colony play? *Insectes Sociaux*, 47(4), pp.357–363. https://doi.org/10.1007/PL00001731.
3. King, H., Ocko, S. and Mahadevan, L., 2015. Termite mounds harness diurnal temperature oscillations for ventilation. *Proceedings of the National Academy of Sciences*, 112(37), pp.11589–11593. https://doi.org/10.1073/pnas.1423242112.
4. Karibi-Botoye N. F., Theraulaz G., Muljadi B., Demyanov V. and Singh K. 2025. Termite mound architecture and climate control: a review of X-ray tomography and flow field simulation approaches. *J. R. Soc. Interface*, 22: 20250263. https://doi.org/10.1098/rsif.2025.0263.
5. Schmidt, R.S., 1955. Termite (*Apicotermes*) nests: Important ethological material. *Behaviour*, 8(4), pp.344–356.
6. Noirot, C. and Darlington, J.P.E.C., 2000. Termite nests: Architecture, regulation and defence. In: T. Abe, D.E. Bignell and M. Higashi, eds. *Termites: Evolution, sociality, symbioses, ecology*. Springer, pp.121–139. https://doi.org/10.1007/978-94-017-3223-9_6.
7. Zachariah, N., Singh, S., Murthy, T.G. and Borges, R.M., 2020. Bi-layered architecture facilitates high strength and ventilation in nest mounds of fungus-farming termites. *Scientific Reports*, 10, p.13157. https://doi.org/10.1038/s41598-020-70058-2.
8. Jost, C., 2020. Nest structure: Termites. In: C. Starr, ed. *Encyclopedia of Social Insects*. Cham: Springer. https://doi.org/10.1007/978-3-319-90306-4_148-1.
9. Martin, S.J., Funch, R.R., Hanson, P.R. and Yoo, E.H., 2018. A vast 4,000 year old spatial pattern of termite mounds. *Current Biology*, 28(22), pp.R1292–R1293. https://doi.org/10.1016/j.cub.2018.09.061.
10. Zachariah, N., Murthy, T.G. and Borges, R.M., 2020. Moisture alone is sufficient to impart strength but not weathering resistance to termite mound soil. *Royal Society Open Science*, 7(8), p.200485. https://doi.org/10.1098/rsos.200485.
11. Constantino, R., 2018. Estimating global termite species richness using extrapolation. *Sociobiology*, 65(1), pp.10–14. https://doi.org/10.13102/sociobiology.v65i1.1845.
12. Nicholas Mark Collins, 1977. The population ecology and energetics of *Macrotermes bellicosus* ismeathmany (Isoptera) Unpublished doctoral dissertation. University of London.
13. Räsänen, M., Vesala, R., Rönnholm, P., Arppe, L., Manninen, P., Jylhä, M., Rikkinen, J., Pellikka, P. and Rinne, J., 2023. Carbon dioxide and methane fluxes from mounds of African fungus-growing termites. *Biogeosciences*, 20(19), pp.4029–4042. https://doi.org/10.5194/bg-20-4029-2023.
14. Ocko, S.A., Heyde, A. and Mahadevan, L., 2019. Morphogenesis of termite mounds. *Proceedings of the National Academy of Sciences of the United States of America*, 116(9), pp.3379–3384. https://doi.org/10.1073/pnas.1818759116.
15. Erens, H., Mujinya Bazirake, B., Mees, P., Baert, G., Boeckx, P., Malaisse, F. and Van Ranst, E., 2015. The origin and implications of variations in soil-related properties within *Macrotermes falciger* mounds. *Geoderma*, 249–250, pp.40–50.
16. Camazine, S., Deneubourg, J.L., Franks, N. R., Sneyd, J., Theraulaz, G., & Bonabeau, E., 2001. Self-Organization in Biological Systems. *Princeton University Press*. https://doi.org/10.2307/j.ctvzxx9tx.

17. Oberst, S.M., Lai, J.C.S., Martin, R. and Saadatfar, M., 2020. Revisiting stigmergy in light of multi-functional, biogenic, termite structures as communication channel. *Computational and Structural Biotechnology Journal*, 18, pp.2522–2534. https://doi.org/10.1016/j.csbj.2020.08.012.
18. Perna, A. and Theraulaz, G., 2017. When social behaviour is moulded in clay: on growth and form of social insect nests. *Journal of Experimental Biology*, 220(1), pp.83–91. https://doi.org/10.1242/jeb.143347.
19. Turner, J.S., 2001. On the mound of *Macrotermes michaelseni* as an organ of respiratory gas exchange. *Physiological and Biochemical Zoology*, 74(6), pp.798–822. https://doi.org/10.1086/323990.
20. Turner, J.S. and Soar, R.C., 2008. Beyond biomimicry: What termites can tell us about realizing the living building. In: *Proceedings of the 1st International Conference on Industrialised, Integrated, Intelligent Construction*, Loughborough, UK, 14–16 May 2008. pp.215–231.
21. Weir, J.S., 1973. *Air flow, evaporation and mineral accumulation in mounds of Macrotermes subhyalinus (Rambur).* Journal of Animal Ecology, 42(3), pp.509–520. https://doi.org/10.2307/3120.
22. Ocko, S.A., Heyde, A. and Mahadevan, L., 2019. Morphogenesis of termite mounds. *Proceedings of the National Academy of Sciences of the United States of America*, 116(9), pp.3379–3384. https://doi.org/10.1073/pnas.1818759116.
23. Schmidt, A.M., Jacklyn, P. and Korb, J., 2014. 'Magnetic' termite mounds: Is their unique shape an adaptation to facilitate gas exchange and improve food storage? *Insectes Sociaux*, 61(1), pp.41–49. https://doi.org/10.1007/s00040-013-0322-6.
24. Korb, J. and Linsenmair, K.E., 1999. The architecture of termite mounds: a result of a trade-off between thermoregulation and gas exchange? *Behavioral Ecology*, 10(3), pp.312–316. doi:10.1093/beheco/10.3.312.
25. Field, M.A. and Duncan, F.D., 2013. Does thermoregulation occur in the mounds of the harvester termite, *Trinervitermes trinervoides* (Sjöstedt) (Isoptera: Termitidae)? *African Entomology*, 21(1), pp.45–57. https://doi.org/10.4001/003.021.0110.
26. Perna, A., Jost, C., Couturier, E., Valverde, S., Douady, S. and Theraulaz, G., 2008. The structure of gallery networks in the nests of *Cubitermes* spp. revealed by X-ray tomography. *Naturwissenschaften*, 95(9), pp.877–884. https://doi.org/10.1007/s00114-008-0388-6.
27. Wango, S.P. and Josens, G., 2011. Comparison of nest shapes and densities of two sympatric species of *Cubitermes* (Isoptera: Termitidae: Termitinae) as clues for the study of their population dynamics. *African Zoology*, 46(1), pp.156–168. https://doi.org/10.3377/004.046.0106.
28. Josens, G., 1971. Thermal variations in the nests of Trinervitermes geminatus Wasmann, in relation to the external environment in the savannah of Lamto (Côte d'Ivoire), *Insectes Sociaux*, 18: 1–13.
29. Singh, K., Muljadi, B.P., Raeini, A.Q., Jost, C., Vandeginste, V., Blunt, M.J., Theraulaz, G. and Degond, P., 2019. The architectural design of smart ventilation and drainage systems in termite nests. *Science Advances*, 5(3), p.eaat8520. https://doi.org/10.1126/sciadv.aat8520.
30. Buades, A., Coll, B. and Morel, J. M., 2008. Nonlocal image and movie denoising. *International Journal of Computer Vision*, 76(2), pp.123–139. https://doi.org/10.1007/s11263-007-0052-1.
31. Buades, A., Coll, B. and Morel, J.-M., 2005. A non-local algorithm for image denoising. In: *Proceedings of the 2005 IEEE Computer Society Conference on Computer Vision and*

781 *Pattern Recognition (CVPR'05)*, Washington, DC, USA, June 20–25 2005. Vol. 2, pp. 60–
782 65. https://doi.org/10.1109/CVPR.2005.38.
783 32. Thermo Fisher Scientific, 2018. *Thermo Scientific™ Avizo™ Software 9 User's Guide.*
784 Waltham, MA: Thermo Fisher Scientific.
785 33. Maes, J. and Menke, H.P., 2022. GeoChemFoam: Direct modelling of flow and heat
786 transfer in micro-CT images of porous media. *Heat and Mass Transfer*, 58(11), pp.1937–
787 1947. https://doi.org/10.1007/s00231-022-03221-2.
788 34. Najafi-Silab, R., Kord, S., Soleymanzadeh, A. and Khaz'ali, A.R., 2023. Assessment of the
789 theoretical models of effective thermal conductivity based on digital rock physics for clean
790 sandstones. *Geothermics*, 114**,** 102803. https://doi.org/10.1016/j.geothermics.2023.102803.
791 35. Kandasami, R.K., Borges, R.M. and Murthy, T.G., 2016. Effect of biocementation on the
792 strength and stability of termite mounds. *Environmental Geotechnics*, 3(2), pp.99–11

Multiscale structural control of airflow, diffusion and heat transfer in non-fungus farming termite mounds

SUPPLEMENTARY MATERIAL

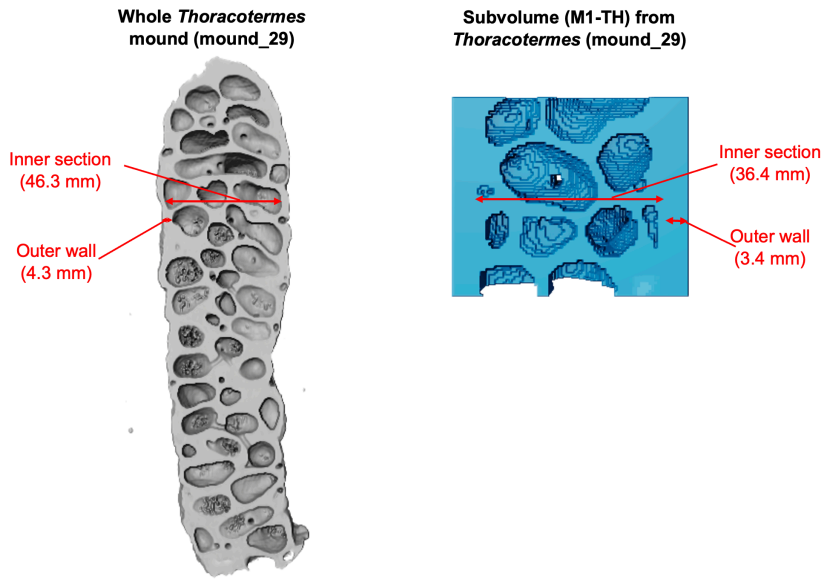

Figure S1: Comparison of the original termite mound geometry and the reconstructed subvolume with the appended outer wall used in the multiscale simulations for *Thoracotermes* (M1-TH). The appended outer wall preserves the original inner section to outer wall thickness ratio (~10.7), observed in the original CT data while allowing effective wall properties obtained from microscale simulations to be incorporated into the mound scale model.

Table S1: Structural properties of the different mound subvolumes obtained from image analysis. The definitions and methods used to compute properties such as Euler number, channel connectivity, and tortuosity are described in Section 3. Here, connectivity refers specifically to channel connectivity at the millimetre scale.

Name of species	Subvolume ID	Channel Porosity	Length in x direction (m)	Volume (m^3)	Average channel thickness (m)	Average inner wall thickness (m)	Channel connectivity	Euler number	Surface area (m^2)	Integral mean curvature	Tortuosity
T. Geminatus	M1-T	0.6	0.11	1.1E-03	5.2E-03	6.9E-03	1.00	-1345	0.31	1.15E+04	1.65
	M2-T	0.6	0.13	1.3E-03	5.5E-03	5.3E-03	1.00	-1358	0.33	1.01E+04	1.51
	M3-T	0.6	0.11	1.4E-03	5.7E-03	4.5E-03	1.00	-1424	0.34	9.62E+03	1.53
	M4-T	0.6	0.1	1.1E-03	5.9E-03	3.9E-03	1.00	-1201	0.28	5.99E+03	1.52
	M5-T	0.5	0.16	8.6E-04	6.8E-03	9.2E-03	1.00	-651	0.18	5.14E+04	1.74
	M6-T	0.5	0.12	5.4E-04	6.9E-03	7.2E-03	1.00	-457	0.12	3.71E+04	1.63
***Cubitermes* spp.**	M1-C	0.5	0.05	1.5E-04	6.5E-03	6.2E-03	0.91	8	0.04	3.46E+04	1.67
	M2-C	0.5	0.05	1.0E-04	6.6E-03	5.1E-03	0.84	39	0.03	2.63E+04	1.8
	M3-C	0.4	0.04	6.9E-05	5.0E-03	5.5E-03	0.97	19	0.02	2.07E+04	1.88
	M4-C	0.5	0.04	2.5E-04	5.8E-03	3.7E-03	0.97	-145	0.09	7.62E+04	1.92
	M5-C	0.5	0.05	1.4E-04	5.7E-03	4.0E-03	0.90	-32	0.05	4.60E+04	1.84
	M6-C	0.6	0.04	6.9E-05	5.9E-03	2.8E-03	1.00	-58	0.03	2.45E+04	1.67
	M7-C	0.5	0.04	7.4E-05	4.1E-03	2.3E-03	0.98	1	0.03	1.15E+05	1.47
	M8-C	0.5	0.04	7.4E-05	4.0E-03	2.4E-03	0.99	-17	0.03	1.18E+05	1.52

Name of species	Subvolume ID	Channel Porosity	Length in x direction (m)	Volume (m^3)	Average channel thickness (m)	Average inner wall thickness (m)	Channel connectivity	Euler number	Surface area (m^2)	Integral mean curvature	Tortuosity
	M9-C	0.8	0.05	1.3E-04	7.0E-03	1.9E-03	1.00	-797	0.05	6.26E+04	1.32
	M10-C	0.7	0.05	9.1E-05	7.0E-03	1.3E-03	0.98	-240	0.04	5.44E+04	1.24
	M11-C	0.7	0.03	2.7E-05	6.4E-03	2.4E-03	0.99	4	0.01	2.14E+04	1.77
	M12-C	0.5	0.05	9.1E-05	4.4E-03	2.3E-03	0.95	-90	0.04	7.21E+04	1.66
	M13-C	0.4	0.04	4.3E-05	4.0E-03	2.9E-03	0.93	10	0.02	4.09E+04	1.41
	M14-C	0.7	0.05	9.1E-05	7.6E-03	1.9E-03	0.97	-24	0.04	1.35E+04	1.34
	M15-C	0.7	0.05	1.3E-04	7.7E-03	2.1E-03	1.00	-21	0.05	1.62E+04	1.66
	M16-C	0.3	0.04	4.3E-05	6.5E-03	6.8E-03	0.67	34	0.01	5.23E+03	1.74
Apicotermes lamani	M1-A	0.8	0.07	3.9E-04	6.2E-03	3.1E-03	1.00	-1112	0.12	1.24E+04	1.09
	M2-A	0.8	0.08	4.4E-04	5.8E-03	2.0E-03	1.00	-1364	0.14	5.91E+03	1.11
***Apicotermes* sp.**	M3-A	0.7	0.07	3.1E-04	4.4E-03	1.6E-03	1.00	710	0.13	3.50E+05	1.05
	M4-A	0.7	0.07	3.1E-04	4.4E-03	1.6E-03	1.00	529	0.13	3.66E+05	1.04
***Thoracotermes* sp.**	M1-Th	0.6	0.04	4.8E-05	8.7E-03	2.6E-03	0.96	18	0.02	2.28E+04	1.43
	M2-Th	0.6	0.03	3.9E-05	8.4E-03	2.9E-03	0.94	17	0.01	1.81E+04	1.33
	M3-Th	0.6	0.03	2.3E-05	7.5E-03	3.4E-03	0.99	18	0.05	1.63E+04	1.5
	M4-Th	0.6	0.05	1.6E-04	5.6E-03	2.6E-03	0.23	117	0.06	2.35E+05	2.11
	M5-Th	0.6	0.05	1.6E-04	5.2E-03	2.4E-03	0.45	27	0.07	2.50E+05	2
Thoracotermes macrothorax	M6-Th	0.5	0.08	4.3E-04	8.1E-03	4.1E-03	0.96	-69	0.11	1.53E+05	1.41
	M7-Th	0.7	0.09	8.2E-04	9.8E-03	2.4E-03	0.99	-775	0.23	2.22E+05	1.22
	M8-Th	0.7	0.09	8.2E-04	9.9E-03	2.1E-03	0.99	-1287	0.24	1.97E+05	1.23

Name of species	Subvolume ID	Channel Porosity	Length in x direction (m)	Volume (m^3)	Average channel thickness (m)	Average inner wall thickness (m)	Channel connectivity	Euler number	Surface area (m^2)	Integral mean curvature	Tortuosity
	M9-Th	0.7	0.1	9.7E-04	9.8E-03	2.0E-03	1.00	-1121	0.29	2.54E+05	1.24

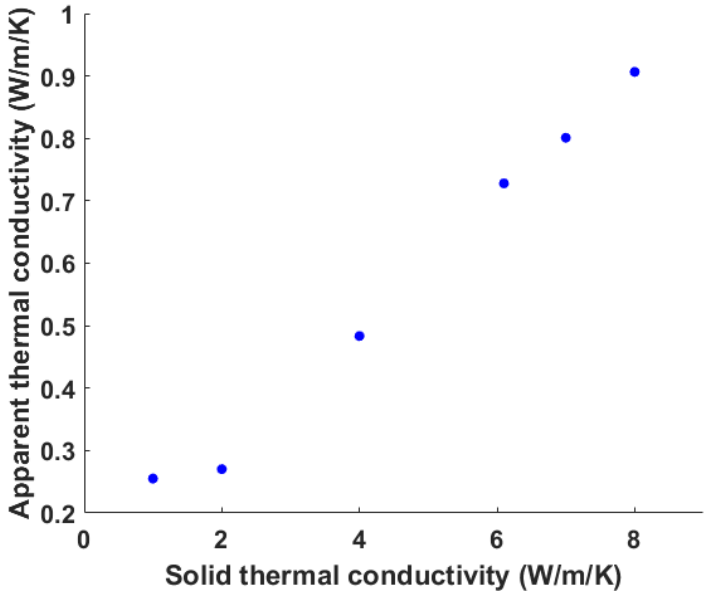

Figure S2: Influence of solid thermal conductivity of mound on thermal conductivity of the entire mound. The solid thermal conductivity values were varied systematically to assess their effect on the overall (apparent) thermal conductivity. The overall thermal conductivity of the mounds was obtained from numerical simulations.

Table S2: Regression diagnostic statistics for the permeability, CO_2 diffusivity and thermal conductivity models

Property	**Shapiro–Wilk p-value**	**White test p-value**	**Maximum variance inflation factor (VIF)**	**Interpretation**
Permeability	0.681	0.775	2.56	Assumptions satisfied
CO_2 diffusivity	0.290	0.792	1.20	Assumptions satisfied
Thermal conductivity	0.538	0.214	1.81	Assumptions satisfied

Residual normality was assessed using the Shapiro-Wilk test, homoscedasticity using the White test, and multicollinearity using variance inflation factors (VIF). For all regression models, the Shapiro-Wilk and White tests were non-significant ($p > 0.05$), indicating no evidence of departures from normality or homoscedasticity. VIF values were below commonly accepted thresholds, 5, indicating that multicollinearity was not sufficiently high to invalidate the regression analyses.

The relationships between structural properties and transport behaviour in the inner sections were quantified using multiple regression analysis, leading to the following empirical correlations:

$$Permeability = 4804.8 \times Porosity^{8} \times Inner\ wall\ thickness^{3.2} \times Connectivity^{2.2} \times Tortuosity^{-4.3} \quad \text{(S.1)}$$

$$CO_2\ diffusivity = 6.7 \times 10^{-3} \times Channel\ Porosity^{2.3} \times Connectivity^{1.3} \times Volume^{0.4} \times Integral\ mean\ curvature^{-0.3} \quad \text{(S.2)}$$

$$Thermal\ conductivity = 5.2 - 0.3 \times Tortousity - 5.3 \times Channel\ porosity - 329.3 \times Volume \quad \text{(S3)}$$